

PAPER

Variable stiffness morphing limb for amphibious legged robots inspired by chelonian environmental adaptations

To cite this article: Robert Baines *et al* 2020 *Bioinspir. Biomim.* **15** 025002

View the [article online](#) for updates and enhancements.



IOP | ebooks™

Bringing you innovative digital publishing with leading voices to create your essential collection of books in STEM research.

Start exploring the collection - download the first chapter of every title for free.

Bioinspiration & Biomimetics



PAPER

Variable stiffness morphing limb for amphibious legged robots inspired by chelonian environmental adaptations

RECEIVED
19 September 2019

REVISED
19 December 2019

ACCEPTED FOR PUBLICATION
8 January 2020

PUBLISHED
13 February 2020

Robert Baines¹, Simon Freeman², Frank Fish³ and Rebecca Kramer-Bottiglio^{1,4}

¹ Department of Mechanical Engineering & Materials Science, Yale University, 10 Hillhouse Avenue, New Haven, CT 06520, United States of America

² Naval Undersea Warfare Center, 1176 Howell St, Newport, RI 02841, United States of America

³ Department of Biology, West Chester University, 730 S High St West Chester, PA 19383, United States of America

⁴ Author to whom any correspondence should be addressed.

E-mail: rebecca.kramer@yale.edu

Keywords: soft robotics, amphibious robotics, amphibious locomotion, variable stiffness, morphing limb, turtle, tortoise

Supplementary material for this article is available [online](#)

Abstract

Robotic vehicles capable of transition from aquatic to terrestrial locomotion face considerable challenges associated with propulsive efficiency and performance in each environment. Here we present a morphing amphibious robotic limb that combines the locomotor adaptations of sea turtles for swimming and tortoises for walking. The limb can transform between the streamlined morphology of a sea turtle flipper and the load-bearing geometry of a tortoise leg using a variable stiffness material coupled to a pneumatic actuator system. Herein, we describe the fabrication and characterization of the morphing limb, and quantitatively show how morphing between hydrodynamic and axial-load bearing states can enhance the locomotive performance of a single design over land and in water.

1. Introduction

1.1. State of the art: amphibious robot propulsive mechanisms

Bioinspired amphibious robotics is a field that may offer transformative performance in navigating the particularly challenging transition between movement in water and on land, including a zone that often encompasses high-energy wave action, heterogeneous substrate types, and dynamically fluidized sediment. The paucity of literature concerning amphibious robots is due in part to the fundamental challenges of designing and integrating together propulsive mechanisms for effective water and land-based locomotion. For instance, a conventional design for amphibious robot propulsive mechanisms utilizes propellers or fins and a separate wheel transmission system to navigate on land and in water, respectively [1–3]. Although functional, this design strategy is burdened by mechanism weight and complexity, inadequate ground clearance, the inability of wheels to traverse unstructured terrain, and the inability of propellers to function effectively in very shallow, fluidized sediment environments.

An examination of biological solutions to transiting between aquatic and terrestrial locomotion suggests that morphological compromise for high performance locomotion in both environments has not yet occurred [4]. However, highly derived species are well-adapted to a specific environment, often at the expense of locomotion in the other (i.e. fish in water, cheetahs on land). In designing a synthetic system, there is an opportunity to combine disparate locomotion modes specialized for a certain environment. Here, we propose that the combination of lift-based swimming and legged walking are promising for bioinspired amphibious robotic design since efficiency in water, terrestrial maneuverability, and the ability to carry significant weight could be achieved simultaneously.

Robotic propulsive mechanisms inspired by the bodily structure and locomotion strategies of snakes, salamanders, and stingrays leverage coupled oscillation of interconnected modules to move both in water and on land [5–8]. However, such robots do not have the capacity to bear large payloads due to size limitations of the modules composing their bodies and the mechanical drawbacks of undulatory propulsion over land.

Robots utilizing limbs as propulsive mechanisms possess the capacity to bear larger payloads than oscillating-type robots and the ability to navigate unstructured or uneven terrain, as opposed to wheeled robots. One amphibious quadruped robot featured limbs with passively retracting flippers that enabled both drag-based swimming and a traditional quadruped-style walking [9]. Similarly, another robot possessed limbs that consisted of flexible, flat plates constrained within thin wire cages that served both as a wheel and a paddle [10]. Though they stand as benchmarks for clever mechanism design, these limbs had fixed structures and stiffness that precluded the capability to tune the propulsive mechanism for more effective locomotion in a particular environment. In addition, though paddling can be advantageous for navigation in shallow water, it is not an efficient mode of submerged swimming, as thrust is only generated over half of the stroke [4].

The ability to vary overall limb stiffness and structural shape confers substantial benefits in nature. The two environments in question here (i.e. terrestrial and aquatic) fundamentally require propulsive limb types to yield at different stiffnesses through variation in material properties and/or structural forms. On land, limb systems must be stiff enough so as to enable the transfer of body weight to a point on the ground without buckling. In water, limbs serve primarily as hydrodynamic surfaces, and must at least partially yield to pressure gradients created by propulsive movements so as to limit stall and the reduction of lift-based thrust. The optimal structural shape and response to loading in each environment is thus fundamentally different. Forms capable of supporting point loads are optimal for terrestrial locomotion, as they maximize grip through pressure friction. Conversely, sleek forms that can sustain distributed hydrodynamic loads and maintain lift-based propulsion are optimal underwater. We therefore contend that for a single limb to approach optimality for both environments, some controllable variation in shape, and thus geometric stiffness, is required.

One group explored changing a propulsive mechanism's structure from a walking configuration to a swimming configuration using toggle-locking rigid segments [11]. While the reported mechanism was capable of structural variation, it was restricted to a set stiffness in its leg and flipper modes and consequently could not leverage the full energetic benefits that could be derived from variable stiffness, as animals do when locomoting and interacting with obstacles [12, 13]. Toward this end, recent work showcased a robot with variable stiffness limbs that allowed it to move effectively across different types of terrain [14]. A human was required to manually adjust the limbs and thus the robot could not change the stiffness with which it interacted with the environment autonomously and *in situ*.

Examples in literature point to a common theme: the viability of amphibious robotic designs hinges on the mechanical capacity to efficiently adapt to land, transitional environments, and water. No reported propulsive mechanism has fully addressed the multiple factors—payload capacity, unstructured terrain navigation, variable stiffness, minimal complexity—that together make a successful design an elusive challenge. New propulsive mechanisms must be designed to accommodate both changes in structure and stiffness without the need for hands-on intervention.

1.2. Chelonian limb adaptations as biological inspiration

Considering the challenge of developing an amphibious propulsive mechanism that is capable of significant structural and stiffness changes, we observed the distinct limb morphologies of two groups of turtles in the order Testudines: testudinidea (Tortoise) and Chelonioida (Sea Turtle) (figures 1(a) and (b), respectively). Each of these animals' limbs exhibits unique locomotor adaptations for their primary habitation environments (i.e. terrestrial/shallow-water and open ocean, respectively).

For example, the turtle leg in the top view of the 3D scan in figure 1(a) features an elliptical cross-section and low aspect ratio ($l_2/t = 1.77$). This adaptation enables the limb to bear greater loads when upright during walking, when turtles and tortoises experience a localized force applied by the ground, F_{env} . A combination of geometric stiffness (the cylindrical shape) and material stiffness (bone and tissue) in the limb allows tortoises to bear and walk under F_{env} energetically efficiently, albeit slowly, over varying terrain [15, 16]. In fact, freshwater turtle bones were shown to be excessively reinforced relative to the loads they and other tetrapods would normally encounter [17]. However, land-based tortoises are incapable of diving and submerged swimming. Freshwater turtles, with legs of similar aspect ratio to that of the tortoise, have diminished top locomotor speed and energetic efficiency in comparison to sea turtles, though this comes with the gain of locomotor maneuverability [18, 19].

In contrast to freshwater turtle and land tortoise limbs, the connective tissue and bone structures in sea turtle flippers are functionally fused into a single high aspect ratio ($l/t = 5.98$ from the Front View of figure 1(b)) hydrofoil ideal for locomotion through water with minimal drag and efficient thrust production [20]. During normal swimming, sea turtles utilize a lift-based locomotion scheme by varying the angle of attack of their flippers relative to oncoming flow to dynamically generate forward thrust and actively mitigate stall [19–21]. While a degree of stiffness is retained in the flipper in order to transmit the load applied by oncoming flow, more mechanical flexibility is inherent in this structure both geometrically (thin, hydrofoil-like shape) and materially (thinner, longer bones and cartilaginous structures). Such

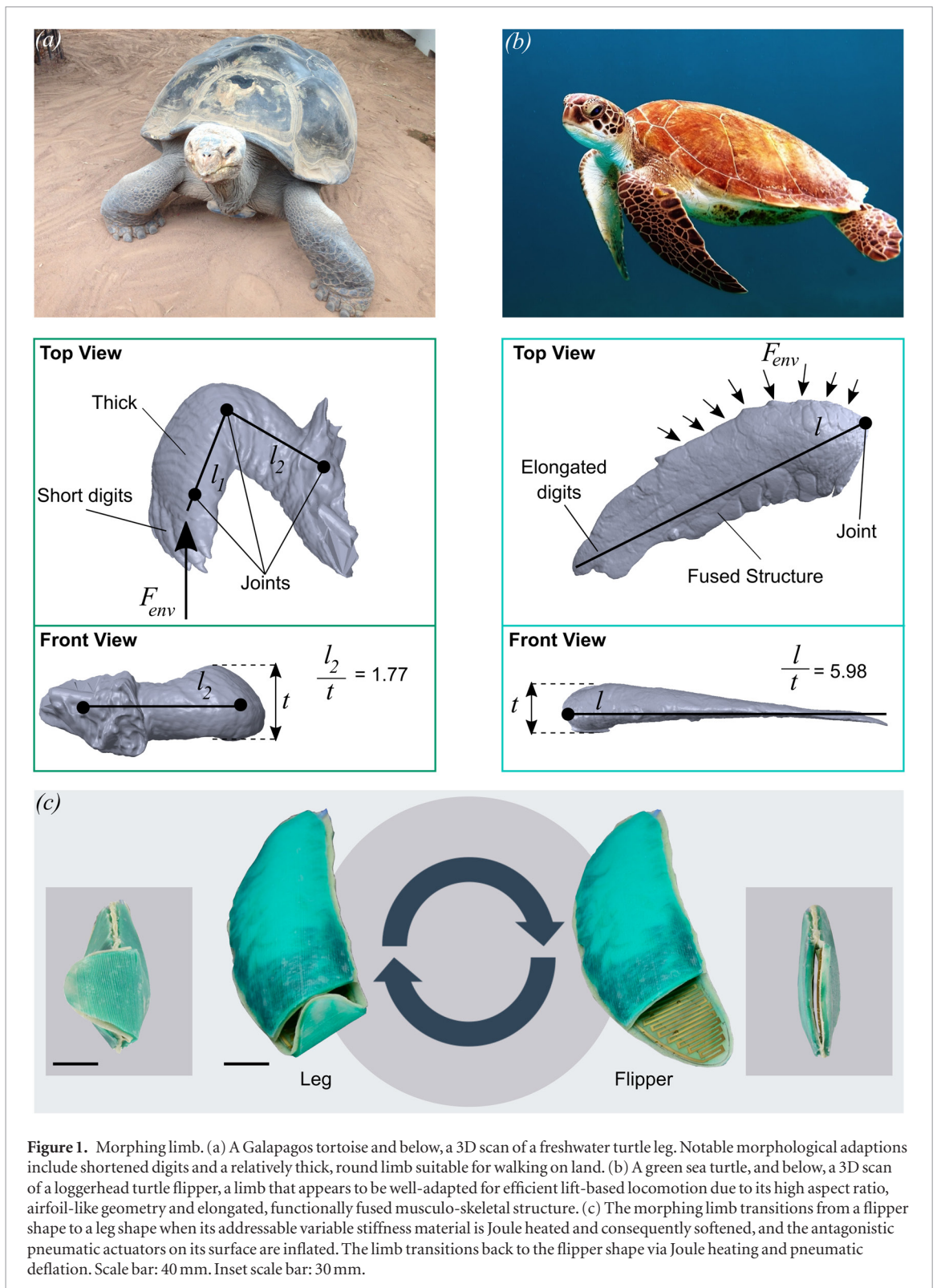
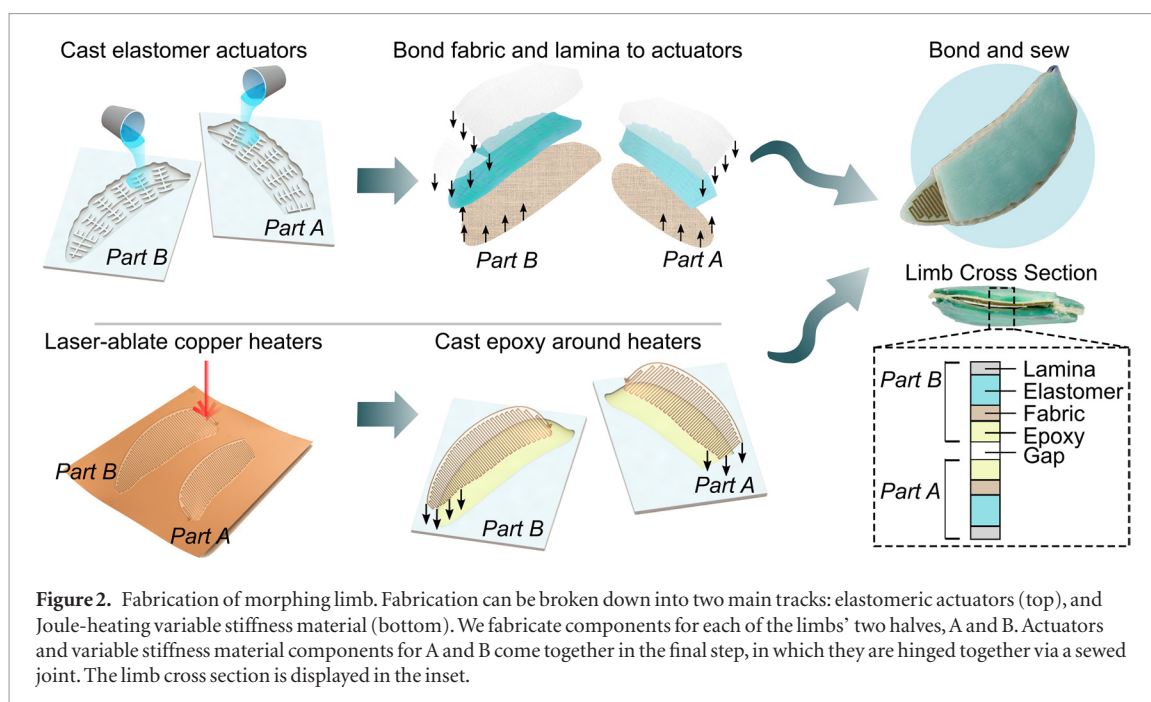


Figure 1. Morphing limb. (a) A Galapagos tortoise and below, a 3D scan of a freshwater turtle leg. Notable morphological adaptations include shortened digits and a relatively thick, round limb suitable for walking on land. (b) A green sea turtle, and below, a 3D scan of a loggerhead turtle flipper, a limb that appears to be well-adapted for efficient lift-based locomotion due to its high aspect ratio, airfoil-like geometry and elongated, functionally fused musculo-skeletal structure. (c) The morphing limb transitions from a flipper shape to a leg shape when its addressable variable stiffness material is Joule heated and consequently softened, and the antagonistic pneumatic actuators on its surface are inflated. The limb transitions back to the flipper shape via Joule heating and pneumatic deflation. Scale bar: 40 mm. Inset scale bar: 30 mm.

relative flexibility enables the turtle limb to respond in a mechanically compliant manner to distributed loads, and delay the onset of flow separation in hydrodynamic scenarios such as an accelerative stroke. In contrast to the propulsive mechanism's prowess in water, however, sea turtles have been described to be clumsy and labored when moving on land [22]. Flipper musculoskeletal structure is not well suited to support the concentrated weight due to gravity of a massive body off of the ground. For instance, the length of the flip-

per would create a large moment under such load and would only be supported by the comparatively small area at the end of the flipper. As a result, sea turtles must drag themselves along the ground on land and demonstrate reduced ability to traverse obstacles [22, 23]. Such flipper-based dragging locomotion, especially over granular media, is prone to slips that impact cost of transport.

Beyond their morphologically distinct propulsors, sea turtles and tortoises share a similar body plan;



notably, they have bony or cartilaginous shells spanning the majority of their bodies and are quadrupeds. Morphological similarity between the animals' bodies suggests that a single turtle-inspired robot chassis could employ either form of propulsor. With these observations in mind, we introduced a proof-of-concept amphibious robot limb which sought to marry the locomotor benefits of sea turtle and land tortoise limbs—streamlined geometry and load bearing capacity, respectively—by morphing back and forth between semblances of these two fundamental shapes [24]. Building on our previous work, this paper details a number of improvements to the original limb, including refined geometry for optimized hydrodynamics in the flipper state, cyclic load stability in the leg state, and a streamlined fabrication process which renders a cohesive, demonstrably water-resistant limb. In this study, the morphing limbs were developed and assessed independently of a robotic platform. We are presently building a robot equipped with the morphing limbs; its locomotive performance will be the subject of future work.

The morphing limb (figure 1(c)) utilizes soft fluidic actuators in an antagonistic configuration and a thermoset epoxy, which serves as a variable stiffness material, bonded to the strain limiting layer between the actuators to permit morphing between flipper and leg states (supplementary video 1 (stacks.iop.org/BB/15/025002/mmedia)). The limb's default state is a flipper. Within the thermoset is an embedded thin-foil copper heater which can Joule heat the thermoset above its glass transition temperature (T_g) to soften it on-demand. Then, the fluidic soft actuators inflate, causing the limb to deform from flipper to leg. Pressure is held until the thermoset cools. Upon releasing pressure, the limb retains the leg shape. The significant cross-sectional area and structural change is captured

in figure 1(c) insets for both leg and flipper states. Heating the limb back up again returns it to the flipper state by thermally relaxing the thermoset. Stored elastic energy in the elastomer actuators also help return it back to the flipper state.

2. Materials and experimental

2.1. Fabrication of morphing limb

Figure 2 illustrates the manufacturing process of the morphing limb. The limb consists of two halves that we call part A and B. Pneumatic elastomeric actuators reside on each side of the morphing limb. The deformation trajectories of the actuators were tailored by changing the geometry of the acrylic molds in which they were cast. For instance, the mold for part A contained an array of chambers with a larger length to width ratio. This forced bending about the length-wise axis, or the long portion of the limb. Part B featured the same chambers as part A, but with additional chambers with greater width to length ratio at the distal end of the actuator to induce curling to make a foot pad for extra stability. The actuators were cast from a silicone rubber (Dragon Skin 10A, Smooth-On) and degassed in a vacuum chamber to eliminate defects.

After curing, the actuators were bonded to a bi-directional strain-limiting fabric on the bottom and an elastomer lamina with unidirectionally embedded fibers, (introduced in our previous publication [25]), on the tops to further direct their deformation. For part A, the truncated actuator, only a single piece of unidirectional elastomer lamina at 0° was used to facilitate further axial-wise bending. For part B, the unidirectional lamina was placed at 90° at the distal end to facilitate curling and 0° for axial-wise bending.

To create the self-heating addressable variable stiffness material, first, the thin foil copper heater was

etched in a ProtoLaser U4 (LPKF laser and electronics) from 0.127 mm thick copper-clad kapton (DigiKey) in a serpentine pattern of traces 2 mm thick to yield a resistance of 1.2 and 2.2 Ω , for parts A and B, respectively. Two wires for positive and negative electrodes were soldered onto the heater. Then, the two-part thermoset epoxy system was cast by mixing 29% wt. Jeffamine D400 (Hunstaman International, LLC), 71% wt. EPON 828 (Momentive Performance Materials Inc.). After mixing and de-gassing the epoxy, we poured it into molds corresponding to actuator parts A and B lined with the thin copper foil heaters to enable on-demand Joule heating. The mold was then placed in an incubator for 12 h at 60 °C, with weights on top to ensure smooth variable stiffness specimens.

2.2. Thermal characterization

The stoichiometric ratio of epoxy to amine, as well as cure temperature, influence thermoset properties like elastic modulus and T_g [26, 27]. We chose to explore stoichiometric ratio as a way to tune the mechanical properties of a thermoset. We conducted dynamic mechanical analysis (DMA) on samples of three different stoichiometric weight ratios (DMA Q800, TA Instruments), holding cure temperature constant at 60 °C, to determine which ratios yielded appropriate stiffness changes for our morphing limb system.

Sample geometries were ensured to be within the ideal measurement range of the DMA; namely rectangular prismatic specimens having 30 mm \times 12.5 mm \times 5 mm dimensions were cast in a mold, and placed in an incubator at 60 °C for 12 h. After curing, samples were removed and placed into a single-cantilever clamp of the DMA with 9.6 in-lbs torque. A 5 Hz sinusoid force input was applied to the samples with strain amplitude of approximately 0.01%. A temperature sweep was conducted between approximately 20 °C and 80 °C at 1 °C min⁻¹. Storage modulus (E'), loss modulus (E''), and damping ($\tan(\delta)$), were recorded every 1 s.

We assessed the capacity of each heater to evenly raise the temperature of the thermoset epoxy in which it was embedded above T_g when Joule heated. While each heater was subjected to 50 W, measurements of the material system were taken with a infrared camera (FLIR) over 30 s. Since the epoxy layer is very thin (1.8 mm) and has a high surface area (13 533 mm²), its surficial heat distribution as captured by the IR camera gives a close approximation of the internal temperature distribution.

2.3. Mechanical testing

We tracked how well the morphing limb held its morphed leg shape in ambient temperature of 23 °C. Two cases were studied: radial and axial loading. For radial loads, experiments were conducted in free resting conditions (no weight) and with 0.5 kg and 1 kg weights applied downward onto the limb. For axial loading, we placed the limb in an Instron 3345 equipped with a 5 kN load cell and applied a 110 N

compression force (estimated force experienced by one leg of a four-legged robot weighing 45 kg). We marked the edges of the limb and tracked them with a high-definition camera, recording Euclidean distance between the markers every 10 s.

Uni-axial quasi-static compression-to-failure tests (Instron 3345 equipped with a 5 kN load cell) were conducted on the morphing limb in both leg and flipper states, while monitoring electrical continuity. We also conducted the same test on the limb in the flipper state while uniformly heated above its T_g in order to study the effects of both geometric and material softening. The loading rate was 40 mm/min. Cyclic compression tests (Instron 3345 equipped with a 5 kN load cell) were conducted on the limb in leg state, reminiscent of conditions it would experience on a legged robot weighing 45 kg. We set the loading rate to 100 N s⁻¹. We performed trials on two specimens: one was subjected to 30% of its ultimate failure force and the other 60% (260 N and 520 N, with lower bounds 26 N and 52 N, respectively).

2.4. Hydrodynamic testing

We measured lift and drag forces on the limb in a laminar flow tank. The flow tank comprises a 1503 Gal recirculating system with dimensions 225 cm (L) \times 45 cm (W) \times 45 cm (H). All of the walls of the test section are smooth optical glass and had minimal impact on the flow development. We mounted the limb on a sturdy scaffolding that straddled the top of the flow tank, placing it out of the wall boundary layer region and in the direct center of oncoming flow. We adjusted the angle of attack of the limb with respect to the incoming flow. Lift and drag force data were acquired by a 6-axis Gamma DAQ F/T Transducer (ATI industrial), considering the component of force in the direction of flow for drag, and the component of force normal to flow as lift. A National Instruments DAQ (USB-6212) was used with a Matlab data acquisition toolbox to record force data. We acquired three data points for each flow rate and angle in both the flipper and leg states. The tested angles were 0 through 60° in increments of 5°. Flow rates ranged from 0.3 to 0.6 m s⁻¹ in increments of 0.1 m s⁻¹.

We conducted a numerical analysis using ANSYS to obtain the 3D flow in the vicinity of the limb as well as ratio of lift to drag forces on the limb. To provide data to compare to experimental results, we conducted tests across the same angles of attack and flow rate conditions as in the experimental setup. This simulation analysis was conducted using a steady state approach. The morphing limb model was imported as an .IGS file that was originally constructed in SolidWorks and represents very closely the dimensions and angles of the physical prototype. We modeled the neighborhood flow domain of interest as a cylindrical control volume with inlet and outlet areas 3.1416 m² and length 2 m. The limb model was positioned directly in the center of the cylinder. Three computational subdomains,

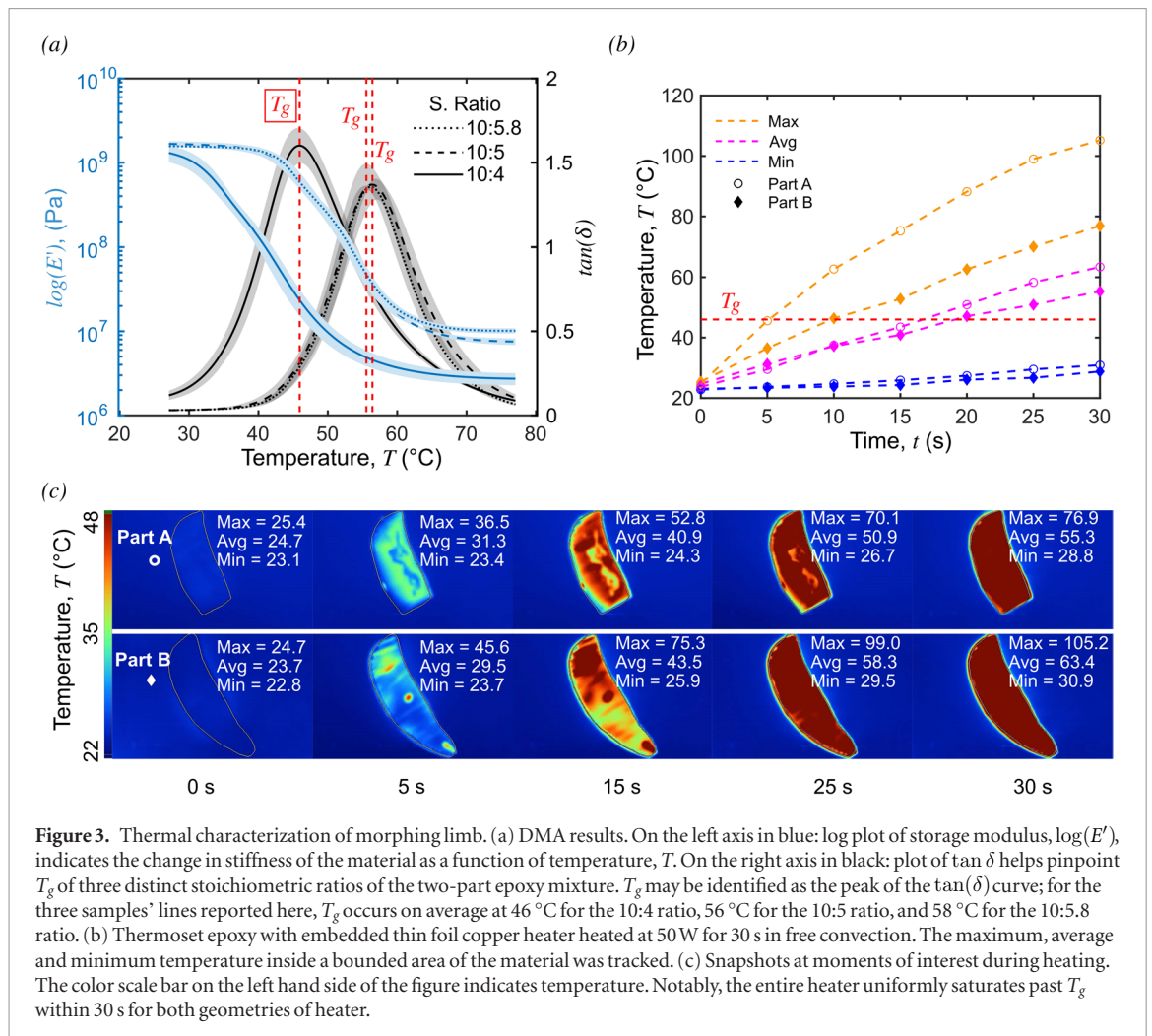


Figure 3. Thermal characterization of morphing limb. (a) DMA results. On the left axis in blue: log plot of storage modulus, $\log(E')$, indicates the change in stiffness of the material as a function of temperature, T . On the right axis in black: plot of $\tan \delta$ helps pinpoint T_g of three distinct stoichiometric ratios of the two-part epoxy mixture. T_g may be identified as the peak of the $\tan(\delta)$ curve; for the three samples' lines reported here, T_g occurs on average at 46 °C for the 10:4 ratio, 56 °C for the 10:5 ratio, and 58 °C for the 10:5.8 ratio. (b) Thermoset epoxy with embedded thin foil copper heater heated at 50 W for 30 s in free convection. The maximum, average and minimum temperature inside a bounded area of the material was tracked. (c) Snapshots at moments of interest during heating. The color scale bar on the left hand side of the figure indicates temperature. Notably, the entire heater uniformly saturates past T_g within 30 s for both geometries of heater.

the inlet, limb surface, and outlet were designated. We utilized a tetrahedral mesh for both the limb and the domain, calculated via the ANSYS 14.0 mesh tool. The entire computational domain consisted of between 500 000 and 1 000 000 cells depending on the parameters, with the density of these cells increasing near the surface of the limb geometry. We utilized the Fluent CFD solver and the solution method scheme was chosen as SIMPLEC. We set the boundary conditions in the simulation to mass flow rate in equal to mass flow rate out of the two faces of the cylindrical domain. The relationship between mass flow rate and the velocity of the experimental test was calculated via:

$$\dot{m} = \rho Av. \quad (1)$$

Here, ρ is the density of the fluid medium (water at 998 kg m^{-3}), A is the area of the face of the cylinder through which the fluid flows (3.1416 m^2), and v is the fluid velocity. We initialized the solution with $v = 0 \text{ m s}^{-1}$ in the direction of flow. Lastly, for convergence criteria, we monitored force of lift and force of drag, as well as the velocity in the flow direction. We set the program to converge and report the ratio of lift to drag forces (F_L/F_D) if all of these metrics reached 0.001 residual value.

3. Results and discussion

3.1. Variable stiffness material thermal characterization

3.1.1. Dynamic mechanical analysis

We wanted to create a variable stiffness material that could be softened on demand to facilitate geometry and stiffness changes of the morphing limb. Thus, we turned our attention to a two-part thermosetting polymer mixture consisting of epoxy and amine. The thermoset provides sufficient stiffness in its cold phase, but when heated beyond its T_g becomes quite compliant.

Figure 3 shows results of the DMA studies we carried out on different stoichiometric ratio samples to identify an appropriate ratio for the morphing limb. Our selection criteria emphasized high stiffness change between soft and rigid phases for distinct limb states, yet a low T_g in efforts to minimize required power input for morphing. Figure 3(a) (left axis) displays the log of the storage modulus ($\log(E')$) of the epoxy specimens as a function of temperature (T), indicating relative stiffness changes between unheated and heated states. Storage modulus (E') quantifies a material's ability to store

energy of deformation elastically. Higher E' means a material is more stiff. On average, the largest stiffness change was attributed to the samples with the 10:4 epoxy to amine ratio, as they started at $E' = 1.2 \times 10^9$ at 25 °C and fell to 2.7×10^6 by 80 °C: nearly a three order-of-magnitude decrease. The specimens with other ratios saw about two orders-of-magnitude in stiffness change. Figure 3(a) (right axis) shows $\tan(\delta)$ as a function of T . The peak ratio of loss modulus to storage modulus, E''/E' , otherwise known as damping ($\tan(\delta)$), is a metric often used to pinpoint T_g in materials whose mechanical response changes with temperature [28]. The peaks of $\tan(\delta)$ reside at 46 °C for the 10:4 ratio, 56 °C for the 10:5 ratio, and 58 °C for the 10:5.8 ratio.

Considering figure 3(a), we opted to use the 10:4 epoxy ratio for the morphing limb variable stiffness material. We made this choice because a lower T_g of 46 °C requires less electrical power input to the heaters for limb transformations. Also, the three three order-of-magnitude stiffness change between unheated and heated states for the 10:4 ratio was the largest witnessed, giving us the widest number of possible stiffness adaptations for the limb.

3.1.2. Joule heating the variable stiffness material

After selecting a stoichiometric ratio for the thermoset epoxy, we cast it in shapes (part A and B) of two sides of the morphing limb and embedded thin copper foil heaters previously discussed in section 2.2. We heated the heater at 50W to ascertain the baseline speed we could expect morphing operations to take place. Figure 3(b) plots the maximum, average, and minimum temperature as a function of time within the contours of the material shown in figure 3(c) for both parts. T_g is indicated by a horizontal dashed red line. The average temperature for each part surpasses T_g within 20 s. Part B reached a higher maximum temperature than did part A, and this occurred at a faster rate.

More insight into the heating over time behavior can be gleaned by observing figure 3(c) and snapshots taken at moments of interest during heating. Despite having consistent material composition, the variable stiffness material cast into parts A and B exhibited unique and localized hot spots, which helps explain the difference between the recorded values of each. For instance, at 5 sec, part A witnessed a steady perimeter-wise aggregation of heat all below T_g , whereas part B had small patches forming that were already well above T_g . Moving on in the sequence to 15 s, parts of both designs exceeded T_g , but were still patchy. We believe heating non-uniformities arose due to slight thickness variations and geometric changes of the copper traces within the material, given they were subject to the same boundary conditions and power input. In spite of variations, by the end, both designs had an average temperature above T_g . We note that extreme edges of the material did not exceed T_g .

With the variable stiffness material fully functional, we moved on to understand the complete limb system's capacity to sustain loads analogous to those it would experience if attached to a walking robot.

3.2. Limb characterization for land-based locomotion

3.2.1. Leg state shape relaxation over time

Maintaining as close as possible to a circular cross section improves the load bearing properties of the limb's leg state. This fact is underscored by observing the ratio between two Euler critical buckling loads, P_{cr} , one for a beam of a hollow circular cross section and one for a hollow rectangular one of equivalent perimeters and thicknesses (representing the flipper and the leg state, respectively):

$$P_{cr} = \frac{\pi^2 EI}{(kL)^2}. \quad (2)$$

Where E is elastic modulus of the variable stiffness material, I is the cross sectional area moment of inertia, k is the length factor (1 for pin boundaries on either side), and L is the unsupported length of the limb. All of these factors except I happen to be the same regardless of limb state. Thus:

$$P_{cr,circle}/P_{cr,rectangle} = I_{circle}/I_{rectangle} \quad (3)$$

$$I_{circle} = \frac{\pi}{4}(r_2^4 - r_1^4) \quad (4)$$

$$I_{rectangle} = \frac{bh^3 - b_1h_1^3}{12}. \quad (5)$$

Solving each in terms of the same set of parameters b , h , and t , we have the ratio:

$$I_{circle}/I_{rectangle} = \frac{\frac{\pi}{4} \left(\left(\frac{2(b+h)}{2\pi} \right)^4 - \left(\frac{2(b+h)}{2\pi} - t \right)^4 \right)}{\frac{bh^3 - (b-t)(h-t)^3}{12}}. \quad (6)$$

From this relation, it is clear that:

$$I_{circle}/I_{rectangle} > 1 \quad \forall (b, h, t) \in \mathbb{R} > 0. \quad (7)$$

Which implies:

$$P_{cr,circle} > P_{cr,rectangle}. \quad (8)$$

Due to the importance of geometric stiffness in our limb system, we inspected the rate at which the leg state's radius decreased as a function of time under constant radial and axial loading. Shape relaxation over time as a result of radial loading could be relevant to, say, a robot floating on the surface of the water, having morphed its limbs into the leg state in preparation for transitioning to land. Radial loads might be induced by water currents or an obstacle pressing against the legs. On the other hand, shape relaxation from axial loading is pertinent to a robot's stability while it is upright, bearing weight.

The results of the radius relaxation tests are summarized in figure 4(a). In the radial loading condition without any weight on top, the leg relaxed by about 40% of its initial radius over a 2.5 h period and had

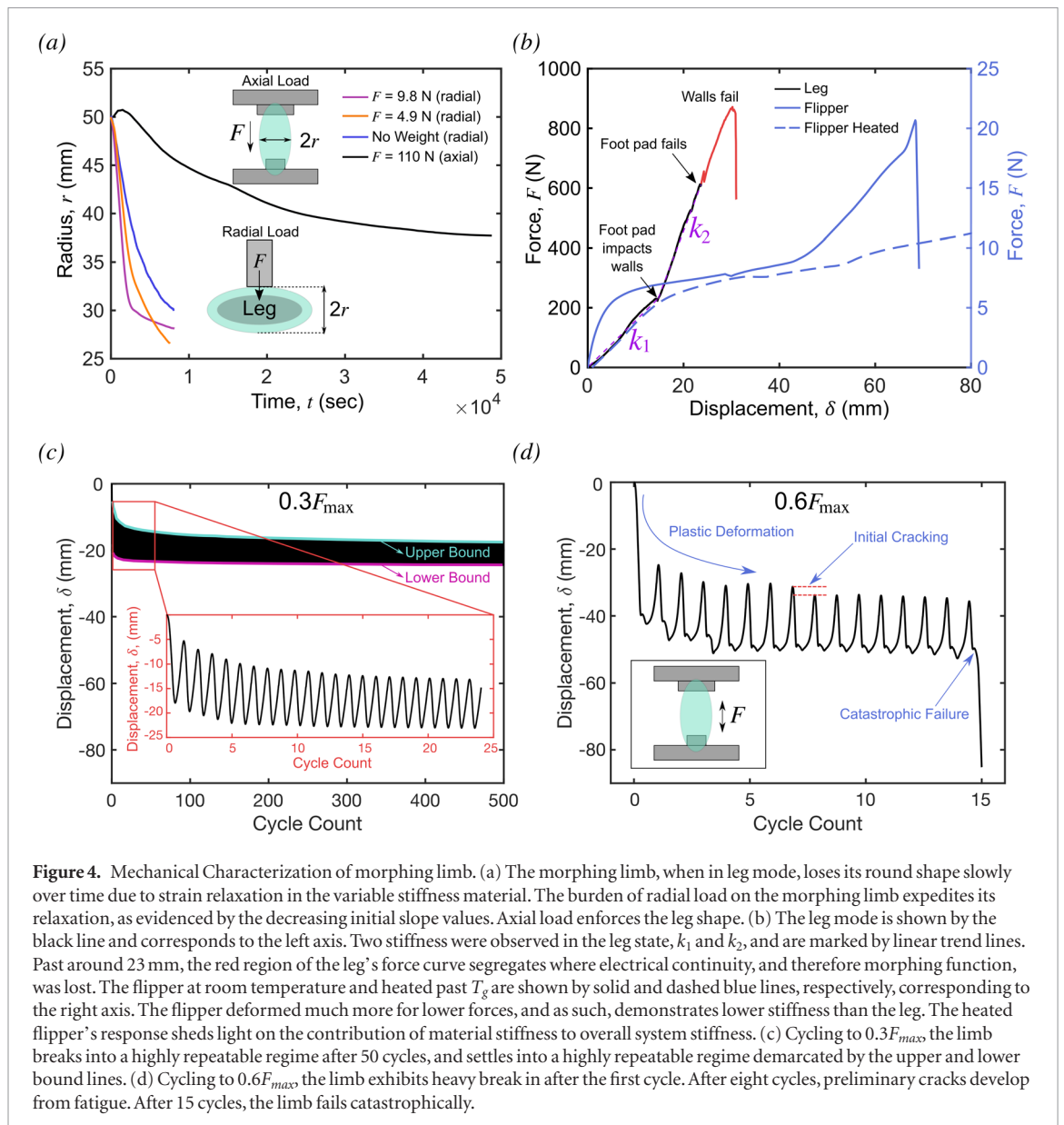


Figure 4. Mechanical Characterization of morphing limb. (a) The morphing limb, when in leg mode, loses its round shape slowly over time due to strain relaxation in the variable stiffness material. The burden of radial load on the morphing limb expedites its relaxation, as evidenced by the decreasing initial slope values. Axial load enforces the leg shape. (b) The leg mode is shown by the black line and corresponds to the left axis. Two stiffness were observed in the leg state, k_1 and k_2 , and are marked by linear trend lines. Past around 23 mm, the red region of the leg's force curve segregates where electrical continuity, and therefore morphing function, was lost. The flipper at room temperature and heated past T_g are shown by solid and dashed blue lines, respectively, corresponding to the right axis. The flipper deformed much more for lower forces, and as such, demonstrates lower stiffness than the leg. The heated flipper's response sheds light on the contribution of material stiffness to overall system stiffness. (c) Cycling to $0.3F_{max}$, the limb breaks into a highly repeatable regime after 50 cycles, and settles into a highly repeatable regime demarcated by the upper and lower bound lines. (d) Cycling to $0.6F_{max}$, the limb exhibits heavy break in after the first cycle. After eight cycles, preliminary cracks develop from fatigue. After 15 cycles, the limb fails catastrophically.

an initial slope of -0.004 . With the addition of external load, the rate increased. With $F = 4.9$ N, we note a steep initial decrease in radius over the first 30 min with a slope of -0.006 , followed by a period of relaxation behavior. Similarly, for $F = 9.8$ N, a steep initial decrease in radius occurred over the first 15 min with a slope of -0.008 . Overall, it decreased by about 60% of its initial radius.

Under axial compression, the rate of radius decrease of the limb was much slower. Even after $12 + \text{h}$ of compression, the axially-loaded leg relaxed by only 20% of its initial radius, and had an initial slope an order of magnitude less than radial load curves: -0.0009 . This result is actually advantageous considering realistic operational conditions—it suggests a robot equipped with the morphing limb and standing upright would have to undergo fewer re-morphing operations to maintain the leg shape. Another phenomenon evident at the beginning of the axial loading curve is a brief increase in leg radius from its starting value. We attribute the initial radius increase of the leg to 'settling in'

due to viscoelastic creep under the compression load. The subsequent decrease is characterized by a gentler slope than the radially loaded conditions.

Physically, the fact that axial compression slowed the radius relaxation could be influenced by two factors: first, being under compression, higher normal forces increased friction at the base of the limb and likely slowed the collapse of the radius as a result of the constrained boundary condition (compare this to the free-end that did not have to overcome any friction by sliding across a substrate in the radially loaded condition). Second, stresses oriented radially due to the compression of the leg combat the relaxation of the material.

The results of radius relaxation experiments suggest the morphing limb will have to be periodically re-heated and re-inflated during normal operation to maintain its optimal leg geometry. The optimal time scale of the repeated re-heat and re-inflate operations depends on the robot's task, environment, and loading conditions.

3.2.2. Leg and flipper states compression to failure

Important factors to consider when implementing the morphing limb on a robot system are the maximum loads it can withstand in its leg state before the leg fails entirely and before it loses morphing functionality. To determine the maximum load the leg state of the morphing limb could tolerate, we conducted a compression to failure test. Results are detailed in figure 4(b) as the black and red line. As the leg state consists of a foot pad at its distal end, the initial compression response of the limb was similar to a low-force spring, providing a compliant response with spring constant $k_1 = 19.53 \text{ N mm}^{-1}$. Once the foot pad had been compressed to the point where it made full contact with the cylindrical walls of the leg, a new stiffness regime more than twice as stiff, $k_2 = 44.25 \text{ N mm}^{-1}$, emerged. Around 23 mm the foot pad cracked and electrical continuity of the heater was destroyed. Finally, at 864 N the limb catastrophically failed because the walls supporting the load fractured and the seam holding the two halves of the limb together ripped out from the fabric.

The max stress seen by the artificial leg can be calculated via:

$$\sigma_{max} = F_{max}/A_{min}. \quad (9)$$

Here, A_{min} is the cross sectional area of the limb at its narrowest point and F_{max} is the max force seen during compression. Note the minimum area on which compression force acts is a thin shell since the interior of the limb in the leg state is hollow. Moreover, the compressive stiffness of the elastomer is negligible in comparison to that of the epoxy. The minimum area can be found by multiplying the limb width by the epoxy thickness and accounting for both halves of the limb with a scaling factor of 2: $A_{min} = 2lw = 2 \times 0.070 \text{ m} \times 0.0018 \text{ m} = 0.000252 \text{ m}^2$.

Plugging in the corresponding F_{max} gathered from the force-displacement graph figure 4(b), yields 3.4 MPa. For a biological comparison, animal bones can have a compressive strength ranging from the same order of magnitude to two orders of magnitude higher than that of our artificial limb [29]. Freshwater cooter turtle leg bones experience peak combined compressive and bending stresses of $31.1 \pm 9.1 \text{ MPa}$ while walking [17]. Although not as strong as its biological counterpart, the maximum sustained load of 864 N by the leg state of the morphing limb is sufficient for a sizable payload-bearing robot.

We also conducted a compression to failure test on the flipper state at 23 °C (room temperature) and heated to 80 °C, indicated by the solid and dashed blue lines in figure 4(b), respectively. The results suggest that the flipper would not perform well in load-bearing applications. Specifically, the flipper at 23 °C exhibited significantly reduced stiffness in comparison to the leg: initially 1.71 N mm^{-1} , and after 5 mm, 0.24 N mm^{-1} . The reduced stiffness caused the flipper to deflect up to a large 70 mm and achieve a relatively

small maximum force of 21 N. Though there was no evidence of catastrophic failure in the variable stiffness material at 70 mm, at this point the flipper was nearly folded in half and slipped substantially in the setup, causing a rapid drop in force. The flipper was plastically deformed to the extent that it did not recover its initial, flat shape when it was extracted from the test setup. At 80 °C, the heated flipper was even less stiff; its initial slope of 0.41 N mm^{-1} is a quarter of that of the flipper at room temperature and underscores the contribution of material stiffness to the overall system stiffness. The heated flipper deflected up to 80 mm, at which point the test was stopped because the flipper had folded onto itself. Electrical continuity was maintained and minimal plastic deformation was evident after extracting and cooling the flipper.

3.2.3. Leg state cyclic compression

Having measured the ultimate load bearing capacity of the leg state of the limb under compression, we sought to study repeated compression emulating a walking motion. Thus, we conducted cyclic compression tests in two conditions: one to 30% and another to 60% of the maximum force seen in figure 4(b). The two conditions were intended to replicate normal working conditions for a 45 kg robot which stands on at least two legs at all times and extreme conditions such as falls or balancing on one leg.

The leg fared for a long duration—the entire 500 cycles of the test—at 30% of the max force. Figure 4(c) displays the results of cyclic loading up to 30% of the max force (260 N). The limb underwent a steady break-in period from cycle 1 up to 50. The rate of hysteresis slowed significantly past 50 cycles, and the drift of the upper and lower bounds of δ was negligible (less than 5%) past 200 cycles. Electrical continuity was still present after the 500 cycles.

Figure 4(d) shows that cyclic loading up to 60% of the max force (520 N) induced substantial plastic deformation within just three cycles. The limb was unable to sustain this higher loading over a long time. Namely, initial crack development occurred at cycle eight, shortly after the initial region of plastic deformation, and is evident as the drop in the upper displacement bound (red dashed lines). After the initial crack, electrical continuity was lost. Crack propagation in subsequent cycles eventually caused the limb to buckle at 15 cycles. Upon inspection of the limb after the test, we noticed the variable stiffness material fractured in multiple locations, including the upper top of the walls by the solder leads and the footpad. Unlike in the compress-to-failure test, the seams mechanically fixing the two halves of the limb together were intact—even after catastrophic failure of the variable stiffness material. This fact suggests the strength of the material was significantly reduced from the high-amplitude cycling so it failed well in advance of the seam.

Land-faring tortoises walk with a duty factor of 0.75, meaning a currently moving limb resides on the

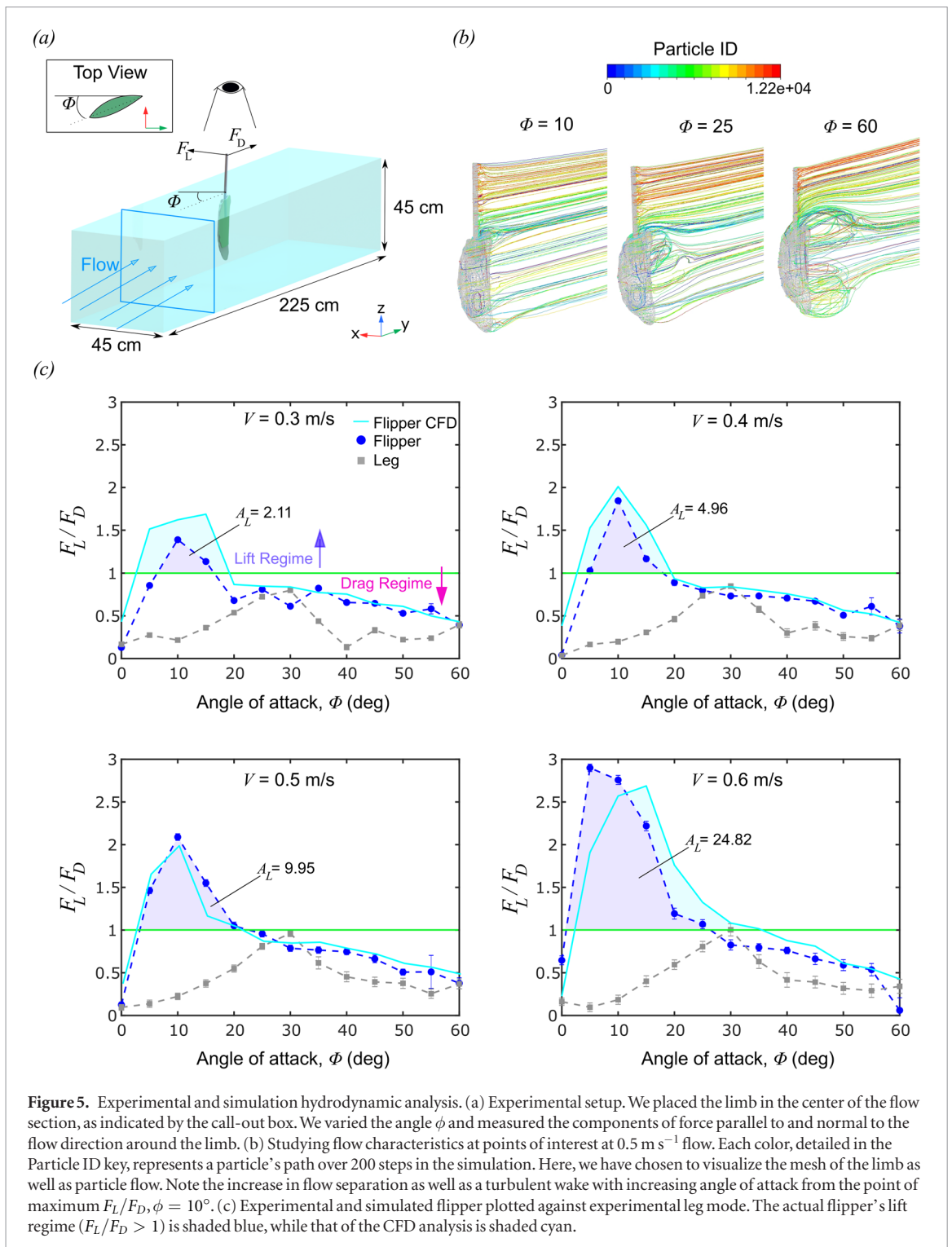


Figure 5. Experimental and simulation hydrodynamic analysis. (a) Experimental setup. We placed the limb in the center of the flow section, as indicated by the call-out box. We varied the angle ϕ and measured the components of force parallel to and normal to the flow direction around the limb. (b) Studying flow characteristics at points of interest at 0.5 m s^{-1} flow. Each color, detailed in the Particle ID key, represents a particle's path over 200 steps in the simulation. Here, we have chosen to visualize the mesh of the limb as well as particle flow. Note the increase in flow separation as well as a turbulent wake with increasing angle of attack from the point of maximum F_L/F_D , $\phi = 10^\circ$. (c) Experimental and simulated flipper plotted against experimental leg mode. The actual flipper's lift regime ($F_L/F_D > 1$) is shaded blue, while that of the CFD analysis is shaded cyan.

ground 75% of the stride duration. Their cadence is also very slow; Galapagos tortoises in particular were shown to take between three and five seconds for a single stride [30, 31]. Consequently, tortoises exert comparable forces when walking as they do when standing still [15, 32]. In the case of our artificial leg, we found that it was able to carry a reasonable robot payload, under assumed normal operation conditions, for 500 cycles, at comparable or faster loading than actual tortoises. Furthermore, it could tolerate up to 60% of its compressive strength to eight cycles, which bodes well for realistic operation conditions, i.e. a robot equipped

with the limb may experience a number of impacts or falls without losing morphing functionality. Having validated the mechanical efficacy of the leg state of the morphing limb, we moved on to assess its hydrodynamics in both leg and flipper states.

3.3. Limb characterization for water-based locomotion

3.3.1. Limb lift and drag measurements

Figure 5(a) illustrates the experimental setup for testing the hydrodynamic properties of the morphing limb. Experiments were conducted between 0.3 m s^{-1} and

0.6 m s⁻¹ free-stream flow velocity. As a comparison, sea turtles swim normally around 0.278 m s⁻¹ but can engage in fast bursts of 0.53 m s⁻¹ or higher [19, 33]. Other work has found that leatherback sea turtles swim most commonly between 0.2 and 0.8 m s⁻¹, and with a maximum value of 2.8 m s⁻¹ [34].

From simulation, we visualized stream lines across the morphing limb at particular angles of interest at a fixed velocity of 0.5 m s⁻¹, shown in figure 5(b). These included: $\phi = 10^\circ, 25^\circ$, and 60° , representing angles of maximum F_L/F_D , stall onset, and bluff body dynamics (lowest tested F_L/F_D), respectively. Figure 5(b) qualitatively displays the effect of the flippers' limited chord length on the flow structure. As the ϕ is increased, tip vortices above and below the main hydrofoil test section become more pronounced. At higher ϕ values, these vortices interact with turbulent flow originating from the low pressure face of the flipper, creating a post-stall flow field broadly similar to what is produced by a delta-shaped airfoil [35].

Figure 5(c) compares glide ratio (F_L/F_D) against angle of attack (ϕ) for both flipper and leg geometries experimentally, and includes numerically modeled glide ratio estimates from the flipper geometry. There is good agreement between experiment and simulation, likely owing to the relatively low free-stream velocity magnitudes tested, fine resolution of the CFD mesh, and closely matched geometry of the CAD model to the test hardware. The flipper state of the morphing limb approximated the performance of a conventional hydrofoil, with the optimal angle of attack for lift-based propulsion occurring around 10° – 15° for all tested velocities. Stall, defined here as when F_L/F_D reduces to 1 or less, occurred consistently around 20° . As the velocity of flow increased, the positive glide ratio area (A_L) grew, and the maximum value of the ratio also increased. Optimal free-stream velocity, likely higher than 0.6 m s⁻¹, was not determined due to experimental limitations in testing higher flow speeds. However, stall angle remains relatively unchanged with speed, and F_L/F_D reduced below unity above 30° in all tests regardless of speed.

Post-stall, the relationship between glide ratio and ϕ for the flipper was broadly similar to that of the leg geometry, with the exception of a peak at around 30° . When in the leg state, we observe that there is some variation of F_L/F_D with ϕ , likely due to the fact that the leg does not become perfectly circular in cross-section but retains a 'thick hydrofoil' shape. While F_L/F_D never exceeded 1, a glide ratio maxima consistently occurred at 30° . This observation is consistent with the mechanics of flow around thick airfoils. While these foils are not capable of producing high F_L/F_D values, their curvature helps retain boundary flow over the low pressure face and delays separation until larger angles of attack [36]. Nevertheless, the design of the limb when in the leg state is intended to support terrestrial

locomotion rather than hydrodynamic propulsion. It does not perform hydrodynamically as efficiently as the flipper state; even the highest glide ratio is a factor of two reduced from that produced by the flipper at a given flow speed.

In summary, experimental and simulation flow test results for the morphing limb show that at this scale of size and flow speeds, the flipper state is well-suited for lift-based locomotion, while the hydrodynamic nature of the leg state can be characterized as a thick hydrofoil. An understanding of the stall properties and optimal angle of attack of the flipper, combined with expected F_L/F_D , can assist in the design of a servomotor actuation sequence that optimizes lift-based propulsion at higher speeds.

4. Conclusion and future work

We have introduced an improved morphing limb intended for amphibious legged robots. The limb is fundamentally different than existing amphibious propulsive mechanisms: a controllable ability to vary shape and stiffness enables optimization for drastically different locomotor styles. Considered in tandem, the performance of the morphing limb in the leg and flipper states holds promise in addressing the challenges faced by robotic vehicles transiting between marine and terrestrial environments.

Just as the tortoise leg exemplifies musculo-skeletal evolutionary adaptations ideal for walking bearing a heavy carapace, the robotic limb's leg state was able to sustain large compression forces over hundreds of cycles without buckling. During compression, the limb maintained morphing functionality, which serves as a testament to its efficacy as a propulsive mechanism for walking on land and subsequently transitioning to marine environments. Moreover, like the sea turtle flipper with hydrofoil-like geometry evolved for efficient lift-based propulsion underwater, the flipper state of the morphing limb demonstrated favorable lift-to-drag forces at a variety of angles of attack and flow velocities that are similar to what a real turtle would experience during normal activities. Simulation validated that lift-dominated areas had tight and surface-conforming boundary layer flow and wake turbulence typical of a hydrodynamic shape rather than a bluff body, suggesting the flipper would perform well as a propulsive mechanism for lift-based swimming.

Future work entails the construction of a quadruped turtle- and tortoise-inspired amphibious robot utilizing the morphing limb presented herein. Challenges associated with such a robot include autonomously adapting both the morphology and stiffness of the morphing limb to the terrain or medium the robot senses it is on/in, and controlling the gait actuation sequence of the robot's limbs as it moves on/in the medium.

Acknowledgments

This work was supported by the Office of Naval Research under the Young Investigator Program (N00014-17-1-2604). Certain images (figure 1(b)) in this publication have been obtained by the author(s) from the Pixabay website, where they were made available under the Pixabay License. To the extent that the law allows, IOP Publishing disclaims any liability that any person may suffer as a result of accessing, using or forwarding the image(s). Any reuse rights should be checked and permission should be sought if necessary from Pixabay and/or the copyright owner (as appropriate) before using or forwarding the image(s).

ORCID iDs

Robert Baines  <https://orcid.org/0000-0002-9023-1536>

Frank Fish  <https://orcid.org/0000-0001-5973-3282>

Rebecca Kramer-Bottiglio  <https://orcid.org/0000-0003-2324-8124>

References

- [1] Yu J, Ding R, Yang Q, Tan M and Zhang J 2013 Amphibious pattern design of a robotic fish with wheel-propeller-fin mechanisms: amphibious pattern design of a robotic fish *J. Field Robot.* **30** 702–16
- [2] Yu J, Tang Y, Zhang X and Liu C 2010 Design of a wheel-propeller-leg integrated amphibious robot *Proc. Int. Conf. on Control, Automation, Robotics, and Vision* pp 1815–9
- [3] Li M, Guo S, Hirata H and Ishihara H 2017 A roller-skating/walking mode-based amphibious robot *Robot. Comput. Integr. Manuf.* **44** 17–29
- [4] Fish F E 1996 Transitions from Drag-based to lift-based propulsion in mammalian swimming *Am. Zool.* **36** 628–41
- [6] Crespi A, Badertscher A, Guignard A and Ijspeert A J 2005 AmphiBot I: an amphibious snake-like robot *Robot. Auton. Syst.* **50** 163–75
- [7] Ding R, Yu J, Yang Q, Tan M and Zhang J 2009 CPG-based dynamics modeling and simulation for a biomimetic amphibious robot *Proc. IEEE Int. Conf. on Robotics and Biomimetics* pp 1657–62
- [8] Crespi A, Karakasiliotis K, Guignard A and Ijspeert A J 2013 Salamandra robotica II: an amphibious robot to study salamander-like swimming and walking gaits *IEEE Trans. Robot.* **29** 308–20
- [9] Vogel A R, Kaipa K N, Krummel G M, Bruck H A and Gupta S K 2014 Design of a compliance assisted quadrupedal amphibious robot *Proc. IEEE Int. Conf. on Robotics and Automation* pp 2378–83
- [10] Dey B B, Manjanna S and Dudek G 2013 Ninja legs: amphibious one degree of freedom robotic legs *Proc. IEEE/RSJ Int. Conf. on Intelligent Robots and Systems* pp 5622–8
- [11] Liang X, Xu M, Xu L, Liu P, Ren X, Kong Z, Yang J and Zhang S 2012 The amphiHex: a novel amphibious robot with transformable leg-flipper composite propulsion mechanism *Proc. IEEE/RSJ Int. Conf. on Intelligent Robots and Systems* pp 3667–72
- [12] Braun D J, Howard M and Vijayakumar S 2011 Exploiting variable stiffness in explosive movement tasks *Proc. Robotics: Science and Systems Conf.* pp 8
- [13] Alexander R McN and Bennet-Clark H C 1977 Storage of elastic strain energy in muscle and other tissues *Nature* **265** 114–7
- [14] Zhong B, Zhang S, Xu M, Zhou Y, Fang T and Li W 2018 On a CPG-based hexapod robot: amphiHex-II with variable stiffness legs *IEEE-ASME Trans. Mech.* **23** 542–51
- [15] Wyneken J, Godfrey M H and Bels V 2008 *Biology of Turtles* (New York: CRC Press LLC)
- [16] Jayes A S and Alexander R McN 1980 The gaits of chelonians: walking techniques for very low speeds *J. Zool.* **191** 353–78
- [17] Butcher M T and Blob R W 2008 Mechanics of limb bone loading during terrestrial locomotion in river cooter turtles (*Pseudemys concinna*) *J. Exp. Biol.* **211** 1187–202
- [18] Blob R W, Mayerl C J, Rivera A R V, Rivera G and Young V K H 2016 On the Fence versus all in: insights from turtles for the evolution of aquatic locomotor specializations and habitat transitions in tetrapod vertebrates *Integr. Comput. Biol.* **56** 1310–22
- [19] Davenport J J, Munks S A and Oxford P J 1984 A comparison of the swimming of marine and freshwater turtles *Proc. R. Soc. B* **220** 447–75
- [20] Fish F E 2004 Structure and mechanics of nonpiscine control surfaces *IEEE J. Ocean. Eng.* **29** 605–21
- [21] Davenport J and Clough W 1986 Swimming and diving in young loggerhead sea turtles (*Caretta caretta L.*) *Copeia* **53** 53–7
- [22] Lutz P L and Musick J A 1996 *The Biology of Sea Turtles* vol 1 (New York: CRC Press)
- [23] Mazouchova N, Umbanhowar P B and Goldman D I 2013 Flipper-driven terrestrial locomotion of a sea turtle-inspired robot *Bioinspir. Biomim.* **8** 026007
- [24] Baines R L, Booth J W, Fish F E and Kramer-Bottiglio R 2019 Toward a bio-inspired variable-stiffness morphing limb for amphibious robot locomotion *Proc. IEEE Int. Conf. on Soft Robotics* pp 704–10
- [25] Baines R, Kim S Y, Vasios N, Bertoldi K and Kramer-Bottiglio R 2019 Reconfigurable soft body trajectories using unidirectionally stretchable laminae *Nat. Commun.* **10** 3464
- [26] Palmese G R and McCullough R L 1992 Effect of epoxy-amine stoichiometry on cured resin material properties *J. Appl. Polym. Sci.* **46** 1863–73
- [27] Carbas R J C, Marques E A S, Da Silva L F M and Lopes A M 2014 Effect of cure temperature on the glass transition temperature and mechanical properties of epoxy adhesives *J. Adhes.* **90** 104–19
- [28] Menard K 2008 *Dynamic Mechanical Analysis: a Practical Introduction* (New York: CRC Press)
- [29] Carter D R and Hayes W C 1976 Bone compressive strength: the influence of density and strain rate *Science* **194** 1174–6
- [30] Williams T L 1981 Experimental analysis of the gait and frequency of locomotion in the tortoise, with a simple mathematical description *J. Physiol.* **310** 307–20
- [31] Zani P A, Gottschall J S and Kram R 2005 Giant Galapagos tortoises walk without inverted pendulum mechanical-energy exchange *J. Exp. Biol.* **20** 1489–94
- [32] Leeuwen J L, Jayes A S and Alexander R McN 1981 Estimates of mechanical stresses in tortoise leg muscles *J. Zool.* **195** 53–69
- [33] Standora E A, Spotila J R, Keinath J A and Shoop R C 1984 Body temperatures, diving cycles, and movement of a subadult leatherback turtle, *Dermodochelys coriacea* *Herpetologica* **40** pp 169–76
- [34] Eckert S A 2002 Swimming speed and patterns of gravid leatherback turtles (*Dermodochelys coriacea*) at St Croix, US Virgin Islands *J. Exp. Biol.* **205** 3689–97
- [35] Bertin J and Cummings R M 2009 *Aerodynamics for Engineers* 5th edn (Upper Saddle River, NJ: Pearson Prentice-Hall)
- [36] McGhee R J and Beasley W D 1976 Effects of thickness on the aerodynamic characteristics of an initial low-speed family of airfoils for general aviation applications *Technical Report* No. NASA TM X-72843, National Aeronautics and Space Administration, Langley Research Center, Hampton, VA